13   Surface Physics

T. Greber, M. Hengsberger, J. H. Dil, H. Yanagisawa, H. Ma, M. Morscher, T. Brugger, F. Meier,
D. Leuenberger, B. Slomski, M. Aksak, S. Roth, H. Cun, M. Thomann, D. Böni, C. Janssen,
G. Landolt, M. Hausherr, P. Donà, M. Klöckner, J. Osterwalder

With the growing impact of nanoscience and -technology, surface and interface phenomena have to be understood more and more at the atomic level. The surface physics laboratory is well equipped for the preparation and characterization of clean surfaces, metal and molecular monolayer films, as well as covalently bonded single layers, using a wide variety of experimental techniques. Moreover, we operate two photoemission spectrometers at the nearby Swiss Light Source (SLS), one for spin- and angle-resolved photoemission spectroscopy (SARPES) and one for photoelectron diffraction.

The research carried out during the report period can be grouped into four topics:

- **Monolayer films of hexagonal boron nitride (h-BN) and graphene on metal surfaces**
  Due to their strong intra-layer sp^2 bonds, these two materials form robust and chemically rather inert single layers that couple relatively weakly in the third dimension. The mechanical stiffness of these bonds leads to the formation of regular superstructures when grown on top of metal surfaces with different lattice constants, that can be either flat moiré-type structures, or strongly corrugated layers with interesting functionalities (1; 2; 3). A prominent example is the boron nitride nanomesh that forms upon high-temperature chemical vapor deposition of borazine on Rh(111) (4). Graphene forms corresponding structures on Rh(111) and Ru(0001) but with inverted corrugations (5). Very accurate structural studies of these systems have been carried out in the last year by means of surface x-ray diffraction, in collaboration with a group from PSI (6; 7). These systems are studied in our group within two different contexts. The first one is the synthesis of heteroepitaxial layers of graphene and h-BN with a view on future electronic devices based on graphene. Due to its in sulating properties and similar crystal structure and lattice constant, h-BN might be the ideal "gate oxide". The second context is the exploitation of these corrugated functional layers as templates for the growth of molecular adlayers with defined periodicities (see Sec. 13.1). This second activity is supported by a Sinergia project of the Swiss National Science Foundation, funding a consortium of four different groups. As an important step, the interaction of water molecules with the h-BN nanomesh was studied at low temperature, where the formation of regular nano-ice clusters was observed (8). Due to the inertness of these films, molecular layers can also be deposited directly and much cheaper from solutions. These studies require a large supply of samples. Therefore, a new growth chamber has been designed and built, in which h-BN or graphene films can be grown on entire four-inch Si(111) wafers. The chamber is placed in a new clean-room that has been installed for this project, which will enable us to process such samples further in a dust-free environment.

- **Molecular adsorbates and molecular monolayers**
  In this past year, important steps were taken towards the setting up of a unique infrastructure for the characterization of molecular layers. A consortium of groups from EMPA, UZH, PSI and the universities of Fribourg and Basel have secured the funding for a new beamline PEARL (PhotoEmission and Atomic Resolution Laboratory) at

the SLS. It is currently under construction and will provide new opportunities to combine careful STM studies of molecular layers with synchrotron radiation based studies of local structure and bonding. In parallel, the development of a new type of Mott detector for spin analysis in our photoemission chamber has continued. The device has been built and is currently being tested in a separate vacuum chamber. This device will be used to study spin degrees of freedom in molecular adlayers and their coupling to a ferromagnetic substrate.

- **Ultrafast processes at surfaces**
Four years ago the group received a vacuum chamber equipped with an elliptical display analyzer (EDA) from PSI in order to study the temporal evolution of photoemission patterns with femtosecond resolution. The setup needed some refurbishing, including a new channelplate detector and a new sample manipulator, and has been successfully commissioned in the last year. First photoemission patterns from a Cu(111) surface, using ultraviolet radiation for excitation, could be recorded, and experiments with pulsed laser excitation are currently underway. In the meantime, the photo-induced field emission patterns resulting from tightly focusing a pulsed laser beam onto a sharp tungsten tip could be understood quantitatively (see Sec. 13.3 and Ref. (9)).

- **Spin-resolved photoemission and momentum mapping**
Our spin-resolved photoemission chamber (COPHEE) at the SLS has been in high demand as a general user instrument due to its unique capabilities. The group's own activities were centered around the study of Bi, Pb and Sb surface alloys on Ag(111), where the band filling and the spin splitting can be readily tuned (see Sec. 13.2). Moreover, two older projects dating back several years could finally be completed: (i) the exchange splitting of

three surface states on Ni(111) could be quantified (10), and (ii) the spin-split surface state on Au(111) could be studied on related vicinal surfaces. The spin polarization and the spin texture in these latter states was found to be surprisingly robust against scattering in periodic step lattices, even in the presence of disorder (11). Spectacular results were obtained in collaboration with a group from Princeton University on a novel class of materials, so-called *topological insulators*. For the first time, the spin polarization of their topologically protected surface states could be measured, and their spin helicity around the Fermi surface was established (12).

[1] T. Greber, http://arXiv.org/abs/0904.1520 (2009).

[2] S. Berner et al., Angew. Chem. Int. Ed. 46, 5115 (2007).

[3] J. H. Dil et al., Science 319, 1824 (2008).

[4] M. Corso et al., Science 303, 217 (2004).

[5] T. Brugger et al., Phys. Rev. B 79, 045407 (2009).

[6] D. Martoccia et al., Surf. Sci. 604, L9 (2010).

[7] D. Martoccia et al., Surf. Sci. 604, L16 (2010).

[8] H. Ma et al., Chem. Phys. Chem. 11, 399 (2010).

[9] H. Yanagisawa et al., Phys. Rev. Lett. **103**, 257603 (2009).

[10] T. Okuda et al., Phys. Rev. B, 80, 180404(R) (2009).

[11] J. Lobo-Checa et al., Phys. Rev. Lett., to appear (2010).

[12] D. Hsieh et al., Nature 460, 1101-1106 (2009).

In the following, three highlights of last year's research are presented in more detail.

13.1 Switching surface texture by hydrogen intercalation

In collaboration with: M. Iannuzzi and J. Hutter, Physikalisch-Chemisches Institut, Universität, Zürich; A. Winkler, Institut für Festkörperphysik, Technische Universität Graz, Austria.

Intercalation – that is the reversible embedding of atomic or molecular species into a layered material – is a key concept for materials functionalization. Graphite is the prototype intercalation material in which the relatively weak bonding between sp^2-hybridized carbon sheets allows the packing of molecular species between subsequent layers. We address the question whether intercalation is also possible between single sheets of carbon (graphene) or h-BN and the supporting metal surface, and what the effect will be on the

corrugated superstructures that are characteristic of these systems (1). It is found that the surface texture of the h-BN nanomesh on Rh(111) may be reversibly switched from corrugated to flat by intercalation of atomic hydrogen, and back to corrugated by hydrogen desorption (2).

The topographic STM data in Fig. 13.1a show that after exposure to atomic hydrogen, a new phase of single layer h-BN without superstructure corrugation (phase II) can coexist with the unaltered nanomesh (phase I). Phase II is basically flat whereas the pristine nanomesh exhibits a corrugated hexagonal surface texture with a periodicity of 3.2 nm. In the textured phase I region (Fig. 13.1b) several nanomesh unit cells are seen with their distinctive topographic elements, the *holes* ('H', tight bonding) and the *wires* ('W', loose bonding). The zoom into the untextured region is
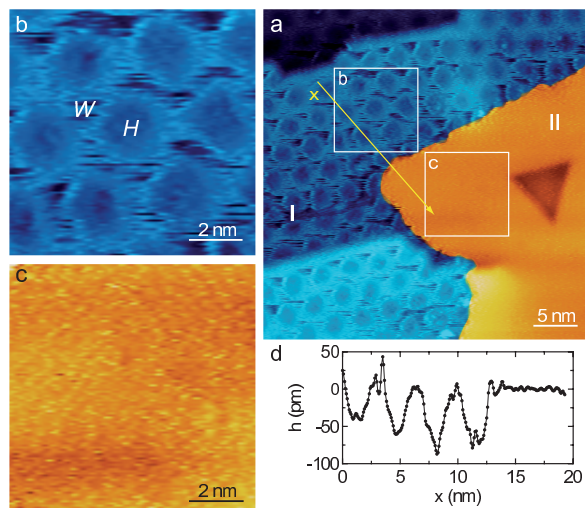

Figure 13.1: Topographic scanning tunneling microscopy (STM) data of h-BN/Rh(111) after exposure to atomic hydrogen. (a) Large scale image showing the coexistence of corrugated and flat h-BN/Rh(111) (regions I and II, respectively). (b) Zoom into the pristine h-BN/Rh(111) area showing the wire (W) and the hole (H) regions. (c) Zoom into the flat, hydrogen intercalated h-BN/H/Rh(111) area. (d) Line profile along the line in a) showing the transition from corrugated (I) to flat (II) h-BN/Rh(111).
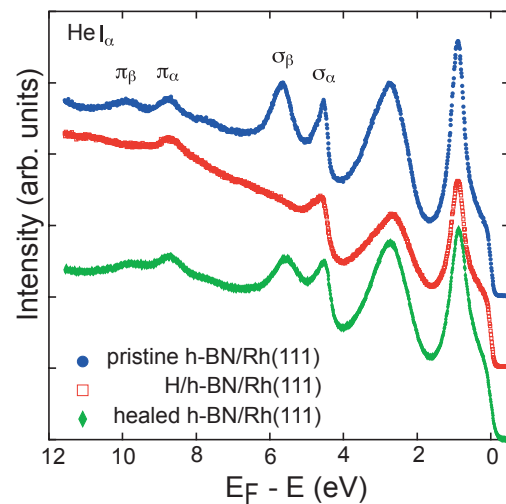

Figure 13.2: He I$_\alpha$ (21.21 eV photon energy) excited normal emission photoelectron spectra from a h-BN/Rh(111) nanomesh before (filled blue circles) and after (open red rectangles) exposure to atomic hydrogen, as well as after subsequent H desorption (filled green diamonds). They show the vanishing of the σ_β and π_β peaks which are attributed to the hole regions (H) of h-BN/Rh(111) after hydrogen intercalation, while the σ_α and π_α peaks corresponding to the wire regions (W) remain.

basically flat (Fig. 13.1c). The height profile in Fig. 13.1d shows the transition from the corrugated region into the flat region. The film surface in the flat region levels on the height of the wires, i.e. the loosely bonded regions in the nanomesh.

The photoemission spectra in Fig. 13.2 confirm the flattening of the h-BN layer and support the hydrogen intercalation picture: the bands related to the holes of the nanomesh (π_β and σ_β) vanish after extensive H exposure, indicating a complete lifting of the corrugation across the entire surface. Furthermore, annealing of the H exposed sample to about 600 K recovers the original band splitting as the pristine corrugation is restored. Calculated N p_x densities of states (DOS) in the hole and wire sites exhibit pronounced peaks at about 7 eV and 6 eV below E_F, respectively, explaining the experimentally observed σ band splitting of about 1 eV. On the other hand, the N p_x DOS with one monolayer of intercalated hydrogen shows only one pronounced peak roughly at the energy of the wire site, reproducing the experimentally observed disappearance of the hole derived band upon exposure to atomic hydrogen. These results thus confirm that hydrogen intercalates between the film and the metal surface.

The demonstration of reversible hydrogen intercalation in the h-BN/Rh(111) system, and the concomitant lifting and recovery of the surface corrugation, is expected to be a more general phenomenon in these sp^2-hybridized template systems on transition metal surfaces, including also graphene.

[1] T. Greber, http://arXiv.org/abs/0904.1520 (2009).

[2] T. Brugger et al., http://arXiv.org/abs/0911.1317v1.

## 13.2 Unconventional Fermi surface spin textures in surface alloys

In collaboration with: L. Patthey, Swiss Light Source, Paul Scherrer Institute; S. Guerrero and Ch. Mudry, Condensed Matter Theory Group, Paul Scherrer Institute; V. N. Petrov, St. Petersburg Polytechnical University, St. Petersburg, Russia.

At surfaces and interfaces, the space inversion symmetry is broken. The spin-orbit interaction can thus lift the degeneracy of the electronic states via the so-called Rashba effect (1). For a two-dimensional free-electron gas, this effect leads to two fully spin-polarized parabolae shifted away from the $\bar{\Gamma}$-point ($k_\parallel = 0$) in opposite directions by the wave vector k_0. The spin polarization vectors lie in-plane and perpendicular to the momentum k, rotating tangentially around the constant energy contours. This Rashba-type spin-splitting forms the basis of the spin field-effect transistor proposed by Datta and Das (2); it allows for a controlled precession of the electron spin.

The Bi/Ag(111) and Pb/Ag(111) surface alloys form a new class of materials, in which the Rashba-type spin-splitting is dramatically enhanced due to a combination of strong atomic spin-orbit interaction of the heavy metals with structural effects enhancing the local potential gradients at the surface (3; 4; 5). The surface state band structure in Bi/Ag(111) features four spin-split "upside-down" parabolae, forming two Kramers pairs, some of which can be seen in the ARPES data of Fig. 13.3a (x=1). By preparing mixed Bi_xPb_{1-x}/Ag(111) surface alloys, both the Fermi energy and the spin splitting can be tuned, as is shown in the same figure. In particular, there are concentrations x where the Fermi level lies between the apex and the crossing point of the inner Kramers pair (x=0.6). In this region, the Fermi surface topology is changed and the density of states features a Van Hove singularity (see Fig. 13.3h). As a
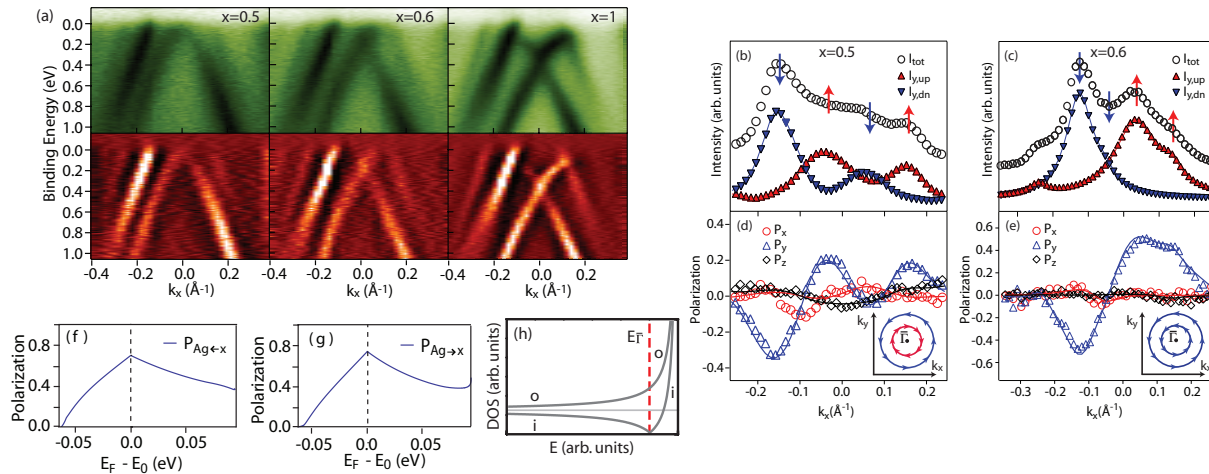
Figure 13.3: (a) Upper graphs: experimental band dispersion of Bi_xPb_{1-x}/Ag(111) surface alloys for varying compositions x (from left to right) along the $\bar{\Gamma}\bar{K}$ direction. Lower graphs: second derivative data. (b) and (c) Total spin integrated intensity (circles) and spin-resolved intensity curves (P_y-projection) measured near the Fermi energy. (d) and (e) are the corresponding measured (symbols) and fitted (solid lines) spin-polarization data. (Insets) Schematically drawn Fermi surface spin textures. (f) Spin polarization of the electron current from the Rashba system to the Ag(111) surface state, calculated within the Drude limit, as a function of $E_F - E_{\bar{\Gamma}}$ and (g) spin polarization of a current flowing in the opposite direction. (h) Density of states for the inner (i) and the outer (o) constant energy textures. (from Ref. [8]).
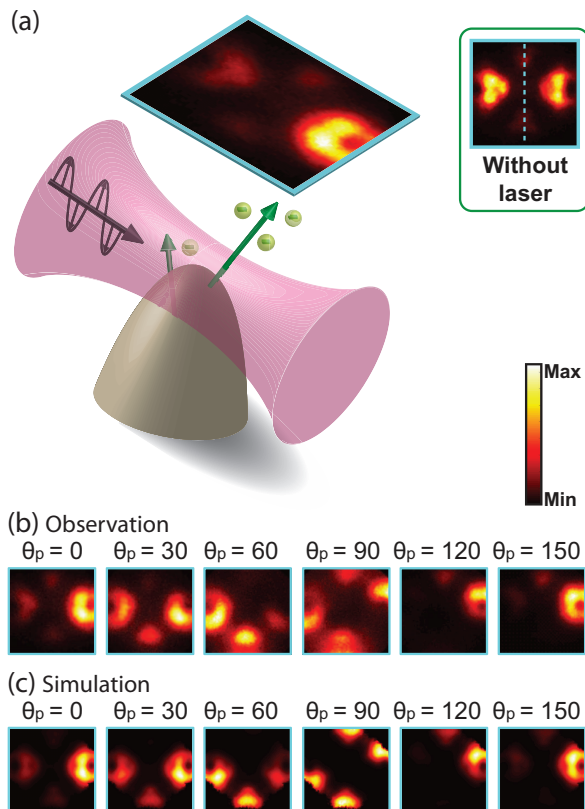
consequence, intriguing physical effects can be expected, among them changes in the Fermi liquid parameters (6), superconductivity transition temperatures (7) and real-space spin accumulation(9).

We have performed spin and angle resolved photoemission measurements of the mixed Bi_xPb_{1-x}/Ag(111) surface alloys with the focus on the inner Kramers pair. The data analysis employed our two-step fitting routine, which allows for a precise determination of the individual spin polarization vectors of the measured states (5). The main results are shown in Fig. 13.3b-e. For x=0.5, we find similar Fermi surface spin textures as observed for Pb/Ag(111), and for Bi/Ag(111) at higher binding energies, i.e. the spins on the two Fermi surface contours are mainly in-plane and point in opposite directions for the inner and outer contours at a given k direction as shown in Fig. 13.3b (and inset) (5). In contrast, for x=0.6 the Fermi surface spin textures are unconventional (see Fig. 13.3c and inset). Each two states crossed on the same side of $\bar{\Gamma}$ now belong to one and

the same Kramers pair and thus have parallel spin polarization vectors and are reversed according to time reversal symmetry when $k \rightarrow -k$.

These findings demonstrate that such Rashba systems can be tuned, while still preserving their high degree of spin polarization. In this context, new prospects for potential applications for spintronics emerge. In Fig. 13.3f and g we show calculated values of the spin polarization for a surface electron current from the Bi_xPb_{1-x}/Ag(111) Rashba system to the Ag(111) surface state (f) and vice versa (g) as a function of the Fermi level position relative to the crossing point $E_{\bar{\Gamma}}$ of the parabolae. Due to the difference of the densities of states deriving from the inner and the outer constant energy contours (see Fig. 13.3h) the current is highly spin polarized, reaching values of almost 80% when the Fermi energy lies at $E_{\bar{\Gamma}}$. Spin-polarized currents can thus be obtained from Rashba type spin-orbit interaction without the use of any magnetic materials.

[1] Y.A. Bychkov and E.I. Rashba, JETP Lett. 39, 78 (1984).

[2] S. Datta and B. Das, Appl. Phys. Lett. 56, 665 (1990).

[3] C. R. Ast et al., Phys. Rev. Lett. 98, 186807 (2007).

[4] D. Pacile et al., Phys. Rev. B 73, 245429 (2006).

[5] F. Meier et al., Phys. Rev. B 77, 165431 (2008).

[6] E. Cappelluti et al., Phys. Rev. Lett. 76, 085334 (2007).

[7] E. Cappelluti et al., Phys. Rev. Lett. 98, 167002 (2007).

[8] F. Meier et al., Phys. Rev. B 79, 241408(R) (2009).

[9] J. Sinova et al., Phys. Rev. Lett. 92, 126603 (2004).

13.3 Optical control of field-emission sites by femtosecond laser pulses

In collaboration with: Christian Hafner, Laboratory for Electromagnetic Fields and Microwave Electronics, ETH Zürich.

Applying strong electric fields to a metal enables field emission due to electron tunneling through the surface potential barrier into the vacuum. Field emission from metallic tips with nanometer sharpness is particularly interesting due to the high brightness and coherence of the resulting electron beams. When a focused pulsed laser beam illuminates the tip, the electric fields of the light wave are enhanced at the tip apex due to the excitation of surface electromagnetic (EM) waves like, e.g., surface plasmon polaritons. Only recently, it was found that the enhanced fields induce pulsed field emission in combination with a moderate DC voltage applied to the tip (1).

We have investigated electron emission patterns induced by femtosecond laser pulses from a clean tungsten tip apex which is oriented along the (011) direction, and compared them with those of field-emitted electrons without laser excitation. The laser light was focused to 4 μm onto the tip apex, and emitted electrons were detected by a two-dimensional detector as schematically depicted in Fig. 13.4a. We observed a striking difference in symmetry of the two patterns (2; 3). Without laser, we observed the typical field emission pattern of a clean tungsten tip as shown in the inset of Fig. 13.4a. With laser, emission sites were the same as those without laser, but the emission intensities become strongly asymmetric between the shadow and exposed sides with respect to the laser pulse, as shown in Fig. 13.4a. Varying the laser polarization angle changes these distributions substantially as shown in Fig. 13.4b, an effect that had not been observed in earlier experiments (1). In effect,

Figure 13.4:
(a) **Schematic diagram of the laser-induced field emission. The emission pattern is observed by a two-dimensional detector. The inset shows the field emission pattern without laser excitation. (b) Observed and (c) simulated laser-induced field emission images for different light polarization angles θ_P, where θ_P is defined by the angle between the tip axis and the polarization vector; $\theta_P = 0$ is when the tip axis is parallel to the polarization vector.**

we have realized an ultrafast pulsed electron source with emission site selectivity of a few ten nanometers.

To reveal the origin of the asymmetric emission patterns, simulations of local fields on the tip apex were performed by using the software package MaX-1 (4), and the resulting local fields were used for simulating electron emission patterns where the field emission from photo-excited nonequilibrium electron distributions were considered. The simulated emission patterns in Fig. 13.4c are in excellent agreement with the experimental data shown in (b). This comparison clearly demonstrates

that the observed strongly asymmetric features originate from the modulation of the local photo-fields at the tip apex (2; 3).

[1] P. Hommelhoff et al., Phys. Rev. Lett. **96**, 077401 (2006).

[2] H. Yanagisawa et al., Phys. Rev. Lett. **103**, 257603 (2009).

[3] H. Yanagisawa et al., Phys. Rev. B **81**, 115429 (2010).

[4] http://MaX-1.ethz.ch